Unmanned Systems, Vol. 10, No. 3 (2022) 289–306

DOI: 10.1142/S2301385022500170

UNMANNED SYSTEMS
https://www.worldscientific.com/worldscinet/us

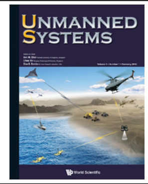

Multi-UAV Coverage Path Planning for Gas Distribution Map Applications

Abdelwahhab Bouras[*], Yasser Bouzid[†], Mohamed Guiatni[‡]

CSCS Laboratory, Ecole Militaire Polytechnique
Bordj El Bahri, Algiers, Algeria

Aerial coverage for Gas Distribution Map (GDM) using Unmanned Aerial Vehicles (UAVs) with olfaction capabilities has become a key for effectiveness and cost improvements. In this work, the main contribution is the application of Coverage Path Planning (CPP) approaches adapted to survey gas plumes using an autonomous fleet of UAVs. Indeed, the mission is carried out in four steps. First, a gas plume model was integrated to simulate the environment. Then, based on the sensor's footprint model and the Voronoï diagram, an exact cellular decomposition method is proposed to generate and distribute measurement points or Points Of Interests (POIs) effectively. To take measurements from all these POIs, two planning approaches were proposed in the third step. One is based on the separation of missions between UAVs using the *K*-means algorithm principle and modeling each path as a Traveling Salesman Problem (TSP). While the second approach models the global mission for all UAVs as a Vehicle Routing Problem (VRP). The resolution of the two mathematical models is achieved using Genetic Algorithms (GAs) and Simulated Annealing (SA) algorithms, respectively. Eventually, the GDM is reconstituted based on triangulation-based cubic interpolation. The evaluation of the proposed simulation techniques based on comparative analyses shows their efficiency, speed and flexibility. The proposed methods take into account the UAV's flight autonomy and the desired coverage quality, and they provide solutions for a variety of coverage applications, particularly for GDM.

Keywords: Multiple unmanned aerial vehicles (multi-UAVs); coverage path planning (CPP); gas distribution map (GDM).

1. Introduction

The increasing development of processors, actuators performance, sensors and the cost of Unmanned Aerial Vehicles (UAVs) has allowed their involvement in a very wide field of applications such as aerial imaging [1, 2], search and rescue operations [3], agricultural and forestry uses [4], aerial manipulation [5], etc. Their flexibility and maneuver's ability permit them to perform more and more in new open issues, thus to replace human being in missions that present major risks, such as cloud boundary monitoring of toxic gases [6], natural disaster management [7], location of nuclear waste [8], etc.

Recently, UAVs with olfaction capabilities have attracted the attention of several scientific researchers, given the added value of their partial or complete participation in interesting tasks, like chemical leak detection [9], pollution assessment [10], environmental monitoring [11], Gas Source Localization (GSL) and mapping [12], etc. Figure 1 shows an example of quadcopters suitable for this purpose.

Usually, this type of task is carried out using a static sensor network well placed within the Area Of Interest (AOI), using sophisticated equipment, which is in general too expensive. However, this configuration is a special case compared to one or more mobile robots (UAVs in the context of this work) equipped with the necessary set of sensors. The navigation throughout this space aims to eliminate, if possible, locate and/or estimate the dispersed quantities, so as to support risk assessment, precautions, intervention, rescue and decision-making operations. The use of UAVs in this kind of application offers several advantages over the risks to human beings and the reduction of the mission cost. Moreover, their hovering and maneuvering ability, especially in damaged and cluttered areas, provides more benefits. Furthermore, the

Received 10 April 2021; Accepted 3 November 2021; Published xx xx xx. This paper was recommended for publication in its revised form by editorial board member, Bin Xin.
Email Addresses: [*]*madjid-bouras@live.fr*, [†]*Yasseremp@gmail.com*, [‡]*mohamed.guiatni@gmail.com*

June 7, 2022 12:06:05pm WSPC/284-US 2250017 ISSN: 2301-3850 2nd Reading

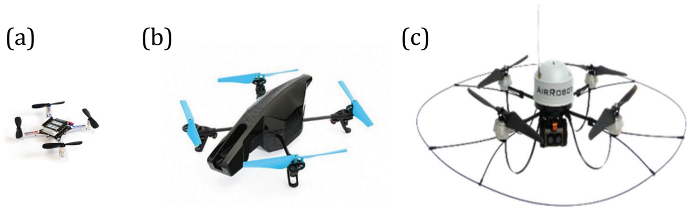

Fig. 1. Example of quadcopters suitable for gas sensing and gas source localization: (a) Nano quadcopter CrazyFlie 2.1. (b) AR drone 2.0 (Parrot SA). (c) Air Robot AR100-B.

employment of UAV swarms gives more efficiency and compensates the autonomy limitation of a single one, as well as it allows them to control larger grounds [13]. However, several improvements are needed for each application, and issues related to energy, control and optimal path planning are raising. The latter plays a major role in the fair and efficient performance of these missions.

In this work, a fleet of UAVs is deployed to survey a toxic gas plume within the AOI. Indeed, the automation of Coverage Path Planning (CPP) is addressed. These UAVs are equipped with electronic noses, making them possible to take a sample from well-defined locations (often called Points Of Interests (POIs)), going from a common starting point (platform) and returning to the same platform. Such a scenario is suitable for collecting data to reconstruct the dispersion map of one or more gas sources in this area. This allows us to provide later additional processing data to estimate the locations of the sources and predict the direction of the chemical's spread.

Papers dealing with Gas Distribution Map (GDM) seek to improve the quality of the gas scattering map, based on probabilistic dispersion models, without optimizing the distance traveled or the energy consumed by the UAV, using in general, a well-structured AOI (square, rectangle, etc.) with reduced dimensions, and only back and forth paths. This path optimization can provide additional data using the same drones that are currently available. Moreover, works on GSL generally focus on one of the sub-questions of the problem (plume finding, plume tracking or source declaration). On the other hand, works including the three phases, despite the improvements introduced to these algorithms, in several cases, the path traveled for search is longer than a pre-defined coverage path for the same AOI, or the latter is more likely to reach the source. Besides the coverage path optimization, CPP algorithms adapted for GSL and GDM have also to take into account a reduced computation time, which calls for simple and effective approaches.

In addition, this type of application requires rapid deployment and effective research, and achieves the mission objectives as soon as possible. In a multi-UAV CPP scenario, the task consists of dividing the efforts among UAVs. Indeed, each drone has to follow the best sequence to visit a finite set of assigned target points. This issue needs a path planning approach that takes into consideration additional constraints, such as limited onboard energy, especially in large areas. Also, the high initial size of the problem, caused mainly by the number of UAVs and the number of POIs, affects the complexity of the problem. The use of effective optimization algorithms in this stage is very useful, especially with multi-UAV.

Motivated by these gaps, the main contribution of this paper is the proposal of an autonomous UAV fleet deployment for gas plume surveillance and mapping in an environment, where many unknown gas sources appear. To the best of our knowledge, this is the first time that multi-UAV CPP has been applied for the GDM, in contrast to what we find in the literature, where each subject is generally treated separately. Integrating a gas plume model, the proposed approach takes into account the gas concentration of the sources and atmospheric stability conditions. To ensure a discrete, full and homogeneous sample of the AOI, a new exact cellular decomposition of the entire AOI into a large number of small cells is adopted, which guarantees automatic generation and distribution of the measurement points (POIs). This step is based on the sensor's footprint model and the Voronoï diagram. Then, two planning methods are proposed to tackle the multi-UAV CPP mission. The coverage is achieved when all measurements are taken without redundancies (passing through all the generated POIs), while respecting the constraints related to the UAVs' flight autonomies. The first approach models the problem as a Traveling Salesman Problem (TSP), after a clustering step using the k-means metric, and it is solved by Genetic Algorithms (GAs). The second models the entire mission as a Vehicle Routing Problem (VRP), and is resolved by the Simulated Annealing (SA) algorithm. A comparative study has been performed to show the efficiency of each approach. Ultimately, based on triangulation-based cubic interpolation, the GDM is reconstituted, which allows us to deduce and estimate the trends of the dispersion of the gaseous sources, and eventually the location of their focus.

The rest of this paper is organized as follows. Section 2 provides a survey of related work on GDM and CPP for multi-UAV. Next, the development of the proposed approaches presenting in detail the compartments of the solution suggested, and describing its algorithms is presented in Sec. 3. Sections 4 and 5 show the parameter setting and discuss comparative results drawn from the simulations, respectively. Whereas Sec. 6 closes the paper with a conclusion and future works.

2. Related Work

This section is divided into two subsections: GDM and multi-UAV CPP. In reality, this choice derives from the fact that, on the one hand, these two subjects are often treated independently in literature. On the other hand, this will allow us to thoroughly study our challenge.

2.1. *Gas distribution map*

GDM is the spatial representation of the gas dispersed amounts from one or more sources. Indeed, the process of synthesizing this map using UAVs includes two phases. Planning pre-defined coverage paths visiting and collecting measurements from specific locations in the environment. Then, an interpolating task of these sampling values to get the estimated dispersion over the entire AOI. Such a map can be exploited for subsequent uses, such as estimating the GSL and making decisions and precautions about the propagation tendency of that chemical substance.

Using this solution (GDM) for GSL as in [14] has advantages over the other alternatives [15–17], such as Gradient-based methods [18], Bio-inspired algorithms [19, 20], which require much time for navigation, and they are strongly influenced by turbulence. Similarly, in Bio-inspired algorithms, the physical sensors used on robots and/or UAVs have degraded performance compared to those of insects and animals. Furthermore, these approaches generally suggest a starting point to find the source close enough to it, and critical situations arise when the information is lost (no gas detection). However, this does not pose problems with the overall coverage of the AOI for GDM. In fact, GDM for GSL is more flexible, well expressed in mathematical formulations and can be adapted to various scenarios. It is more practical for the wind turbulence problem, although it requires a relatively high computational cost. Nonetheless, the development of platforms and their computing capacities have greatly contributed to improving their efficiency.

Besides, the recourse to use multi-agents in these applications has become a promising solution, especially in large areas, despite the challenges posed to ensure their cooperation and optimal path planning. We will analyze this last task in Sec. 2.2, focusing on path planning algorithms for the total coverage of an AOI using a team of UAVs.

2.2. *Aerial CPP for multi-UAV*

The aim of an aerial coverage mission is to gather useful information from several locations. This information can be photographs, measurements, delivery, etc. Indeed, in the case of multi-UAV, each UAV should cover its assigned sub-region by visiting a finite number of POIs (see Fig. 2). The

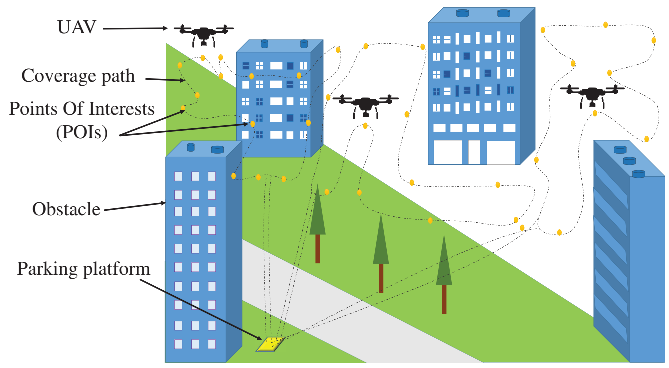

Fig. 2. A synoptic outline of CPP for Gas Distribution Map (GDM) using UAVs.

locations of these points must be well distributed to ensure complete coverage and satisfy certain constraints such as flight time and/or energy consumption, obstacle avoidance, feasibility, etc. that require reliable, flexible and optimal planning algorithms. Most published multi-UAV CPP strategies (especially in the following [21–26]) proceed by four steps as follows:

- The decomposition of the AOI into sub-regions with obstacle isolation using several strategies (e.g. Trapezoidal decomposition, Morse decomposition, Voronoï diagram, etc.).
- Squares, triangles, hexagons, etc. are the usual discretization forms of the sub-regions (got previously) for a good localization and adaptation to the algorithms of the next step. In fact, the decomposition method selected is mainly due to the shape of the sensor footprint.
- A local path planning algorithm that requires a starting cell and a goal cell to deal with the discrete map provided in the previous step. Many strategies have been proposed in the literature, such as grid-based methods (Divide Areas based on Robot's initial Positions (DARPs), Spanning Tree for Coverage (STC), etc.), evolutionary algorithms (Ant Colony Optimization (ACO), multi-ACO), sampling-based methods such as Rapidly exploring Random Trees (RRTs), RRT*, etc.
- A step of smoothing is used to make the planned path feasible by the drones. Generally, this step does not pose a real problem for UAVs with Vertical Take-Off and Landing (VTOL) ability.

Works implementing and testing these techniques in practice are rare [4, 27]. This is due mostly to their high cost. Certainly, many simulations work in literature were developed. Balampanis *et al.* in [28] are solved multi-UAV CPP in three steps: The triangulation of the AOI taking into account the size of the triangle compatible with the used sensor footprint. Then, they have proposed two algorithms called Antagonizing Wavefront Propagation and Reverse

Watershed Schema (AWP & RWS) for the distribution of sub-regions to be covered between UAVs, taking into account the UAVs' flight capabilities, while getting out from nonfly zones by Dead Lock Handling (DLH) algorithm. Avellar *et al.* in [29] place the passage points on the edges of the AOI, in order to synthesize the optimal configuration of straight lines forming back and forth paths while minimizing the mission time. Whereas in [30], path planning is formulated as a VRP in Global Navigation Satellite Systems (GNSSs) challenging environment.

3. The Proposed Methods

The general architecture proposed is summarized in Fig. 3. Indeed, in this section, each compartment of the four blocks will be detailed in an independent subsection.

3.1. *AOI and environment modeling*

3.1.1. *AOI and POIs*

Given the plan at a fixed altitude, in which we will define our AOI and the set of POIs. This working altitude is chosen according to the plume centerline of the chemical dispersion model (Sec. 3.1.2). The AOI is closed and delimited by a set of polygon-shaped segments (convex or nonconvex).

Let $\mathcal{D} \subseteq \mathbb{R}^2$ be our work plan of dimensions $l \times w$. l and w represent the length and the width of $\mathcal{D}$, respectively. Let $\mathcal{A} \subseteq \mathbb{R}^2$ be our AOI defined by a list of n straight segments $\mathcal{S} = \{s_1, s_2, \ldots, s_n\}_{n\geq 3}$, and $\mathcal{A} \subseteq \mathcal{D}$, $\mathcal{O} \subseteq \mathbb{R}^2$ and $\mathcal{O} \subseteq \mathcal{D}/\mathcal{A}$ is the nonfly zone or $\mathcal{O} = \sum_{z=1}^{m} o_z$, such that o_z represents the z^{th} obstacle from m small obstacles located between $\mathcal{A}$ and $\mathcal{D}$. The choice of the set $\mathcal{S}$ is related to the shape and the dimensions of our AOI.

Let $p_i \in \mathcal{A}$ and $p_i = (x_i, y_i)|_{i=1,\ldots,N}$ be the set of our POIs, $p_0 \in \mathcal{A}$ and $p_0 = (x_0, y_0)$ the position of the parking platform of UAVs with coordinates x_0, y_0. The number of passage points (POIs) N is defined in relation to the required coverage. The more the number of these points increases, the better the coverage resolution is. As well as the flight capabilities and the number of UAVs to be used $N_{\text{uav}} \in \mathbb{N}^*$ is defined according to the characteristics of the used UAVs. These UAVs are considered fly at moderate speed without great maneuvers.

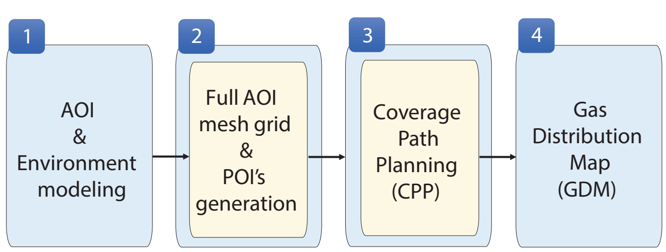

Fig. 3. Architecture suggested.

3.1.2. *Modeling the gas plume*

In this step, we will simulate the gas sources (pollutant or toxic gas, etc.) in order to prepare and reproduce the environment to be probed by the UAVs. Indeed, the presentation of the dispersion emitted by each source on its entourage is the main objective of this subsection. However, some assumptions are used to emulate these gaseous sources, such as constant and steady wind speed, conservation of mass, and no chemical reactions. The resolution of the advection-diffusion equation under these assumptions provides a Gaussian plume equation given as follows:

$$\mathcal{C}(x,y,z) = \frac{\mathcal{Q}}{2\pi u \sigma_y \sigma_z} \exp\left(\frac{-y^2}{2{\sigma_y}^2}\right)\left[\exp\left(\frac{-(z-h)^2}{2{\sigma_z}^2}\right) + \alpha \exp\left(\frac{-(z+h)^2}{2{\sigma_z}^2}\right)\right], \tag{1}$$

where x, y and z are the downwind, crosswind and vertical distances, respectively, $[m]$, $\mathcal{C}(x,y,z)$ is the mean concentration of diffusing substance at point (x,y,z) $[kg/m^3]$. $\mathcal{Q}$ is the contaminant emission rate $[g/s]$, and σ_y,σ_z lateral and vertical dispersion coefficient function $[m]$ (standard deviation). The mean wind velocity in x axe (in downwind) direction is given by u $[m/s]$, h is the effective height of the source $[m]$. Finally, α is the coefficient that characterizes the soil reflection (total reflection for $\alpha = 1$, total absorption for $\alpha = -1$).

This dispersion model is shown in Fig. 4, where the plume is oriented towards the longitudinal x-axis, and the normal distribution of the horizontal and vertical concentration profiles of the plume is shown.

The said model is widely used in the literature [31–33], sight that results are much closer to experimental data and it does not require a supercomputer.

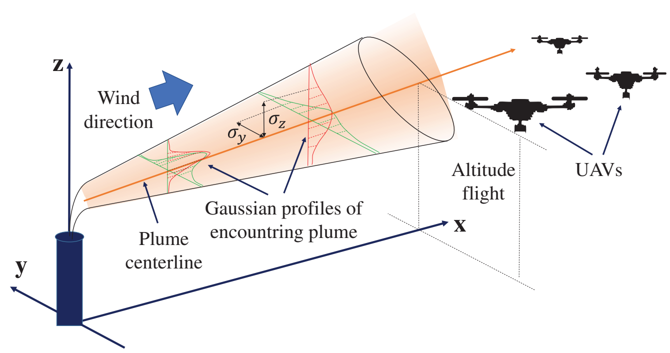

Fig. 4. Visualization of Gaussian plume model and three-dimensional concentration profiles.

Using "Eq. (1)", the effect of variations in the key parameters (atmospheric stability, wind speed, gas emission rate, etc.) generates several envelope forms of the plume dispersion as well as caning, looping, fanning, lofting, etc. [34, 35].

In this model, it is assumed that the plume spread has a Gaussian distribution in both y and z axes. The standard deviation σ_y and σ_z are normally determined based on the six descriptive classes of the atmosphere stability [34, 36]. Going from the classes "A" and "B" which indicate that the atmosphere is extremely and moderately unstable, respectively, to the "E" and "F" classes which indicate that it is slightly and moderately stable, passing by the intermediate classes "C" and "D" (slightly unstable and neutral conditions, respectively).

Various curve fitting routines are used to approximate the standard deviations (σ_y and σ_z). The most frequently used approach is expressed in "Eqs. (2)" and "(3)," respectively, [34]

$$\sigma_y = cx^d, \tag{2}$$

$$\sigma_z = ax^b, \tag{3}$$

where x is the downwind distance from the stack in meters, while a, b, c and d are determined using transformation tables, in which the downwind distance is subdivided into several sections. For each of them, the stability class will have a fixed value of a, b, c and d along this section.

In the same way, it can adjust wind speed to stack height as a function of atmospheric stability class "Eq. (4)":

$$u_z = u_0\left(\frac{z}{z_0}\right)^p, \tag{4}$$

where z and z_0 are the desired and the anemometric height respectively. u_z and u_0 are the wind speed at z and z_0, respectively. p is a dimensionless parameter that depends on the atmospheric stability.

In our work, we consider the following experimental conditions characteristics:

(a) The contaminant is emitted from a fixed height.
(b) The wind speed is constant and coming from the same direction, by supposing the wind does not change comportment during the AOI coverage.
(c) The environmental conditions are selected from the desired stability class, where we will consider "A–B" and "E–F" stability classes according to the appropriately chosen scenarios.
(d) The contaminant with a fixed emission rate.
(e) We consider the soil as a perfect reflector $(\alpha = 1)$.

In Sec. 3.2, we will describe the approach generating our POIs, while ensuring a total and homogeneous sample of this chemical substance along the AOI.

3.2. *AOI discretization and POIs generation*

The POIs generation in the AOI is a very important task. Adequate emplacement has a significant role in defining the chemical substance's dispersion. Indeed, the optimal distribution of these points consists of a uniform and homogeneous allocation that respects a safe distance from the obstacles. For this purpose, the POIs deployment is seen as a mobile wireless sensor network (MWSN), where the performance adopted is the maximization of the degree and the coverage quality. In fact, this depends on the sensing sensor model (sensor footprint) and the desired resolution (with or without overlap (k-coverage)), which define the number of our POIs.

Sensor detection models are subdivided according to their sensing ability into two types: Deterministic (Boolean) sensing model and Probabilistic sensing model. In Boolean sensing model, any event within the sensing range $R_{\max}$ of a sensor-placed in a node- is considered absolutely detected, and not otherwise. Probabilistic sensing model, however, can has a boolean model on a radius $R_{\min}$, and has a given probability on the interval between $R_{\min}$ and $R_{\max}$. Equation (5) gives the coverage function $C(N,\eta)$ of a node N at a point η adopted in this work:

$$C(N,\eta) = \begin{cases} 1 & \text{if } d(N,\eta) \le R_{\min}, \\ \mathrm{Exp}(-\lambda(d(N,\eta) - R_{\min})^{\gamma}) & \text{if } R_{\min} < d(N,\eta) < R_{\max}, \\ 0, & \text{if } d(N,\eta) > R_{\max}, \end{cases} \tag{5}$$

where $d(N,\eta)$ represents the Euclidean distance between node N and point η, and λ, γ are intrinsic parameters of the sensor used.

In our case, the region to be covered has a polygon shape, and its area $\mathcal{A}$ is defined by the following formula:

$$\mathcal{A} = \frac{1}{2}\sum_{i=0}^{n-1}(x_{v_i}y_{v_{i+1}} - x_{v_{i+1}}y_{v_i}), \tag{6}$$

where (x_{v_i}, y_{v_i}) are the coordinates of the polygon vertices (counter-clockwise order), and $(x_{v_{n-1}}, y_{v_{n-1}}) = (x_{v_0}, y_{v_0})$ (closed polygon).

To define the adequate number of POIs, we divide this area over the area of the sensor detection model to be used. That is to say:

$$N_{\mathrm{POIs}} = \frac{\mathcal{A}}{C(N,\eta)\mathcal{A}_{sf}} \times C_r, \tag{7}$$

where $\mathcal{A}_{sf}$ is the area covered by the sensor footprint and C_r is the required coverage rate (k-coverage).

The POIs deployment along the AOI is achieved applying the steps presented in Fig. 5. After introducing the initial

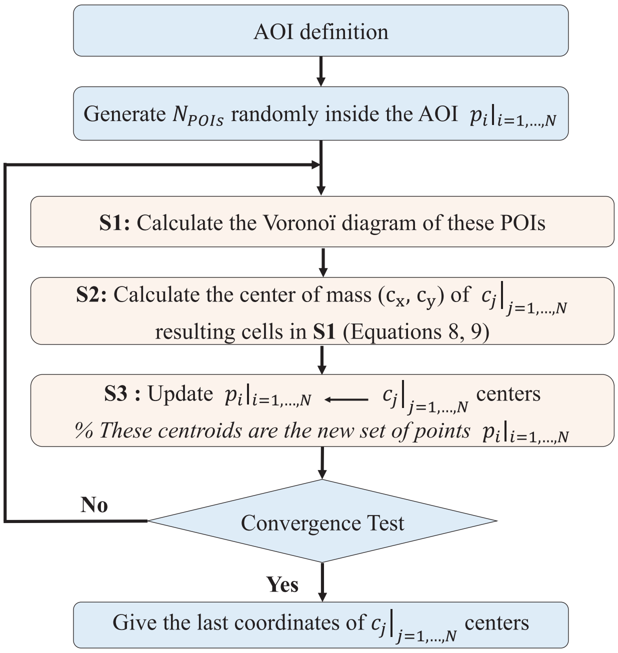

Fig. 5. POIs generation.

data (Map definition, set of points $p_i|_{i=1,\dots,N}$), we divide the AOI into small sub-regions (cells) basing on Voronoï tessellation [37] (S1). Then, we compute the center's coordinates (c_x, c_y) of these $c_j|_{j=1,\dots,N}$ resulting cells (S2) using the following formulas:

$$c_x = \frac{1}{6A_{c_j}} \sum_{i=0}^{n-1} (x_{vc_i} + x_{vc_{i+1}})(x_{vc_i} y_{vc_{i+1}} - x_{vc_{i+1}} y_{vc_i}), \tag{8}$$

$$c_y = \frac{1}{6A_{c_j}} \sum_{i=0}^{n-1} (y_{vc_i} + y_{vc_{i+1}})(x_{vc_i} y_{vc_{i+1}} - x_{vc_{i+1}} y_{vc_i}), \tag{9}$$

where A_{c_j} is the area of the cell c_j calculated using "Eq. (6)", and x_{vc_i}, y_{vc_i} are the coordinates of its vertices.

After that, the set distribution points $p_i|_{i=1,\dots,N}$ is updated with the cell centers $c_j|_{j=1,\dots,N}$ (S3). Finally, a stop test (or an iteration number) is respected when the detection probability $C(N, \eta)$ of each sensor-placed at the centers (c_x, c_y) of the POIs c_j- is maximum (i.e. $C(N, \eta)$ of all sensors does not increase by at least $\pm 1\%$), we consider the last geometric centers calculated as our set of POIs. Otherwise, the three steps are looped, while updating the set distribution $p_i|_{i=1,\dots,N}$. We use the centers $c_j|_{j=1,\dots,N}$ instead.

In this way, the algorithm converges to the construction of almost circular cells, well occupied and/or covered by the sensor's footprints, with uniform distribution in the AOI.

Now, we need to find the adequate paths that ensure a better sequence to visit all these POIs by the UAVs, which is the subject of the next subsection.

3.3. *Coverage path planning*

Recall that our objective is to plan optimal paths for a fleet of UAVs, and connecting all these POIs once each, starting from an initial point and returning to the same point, while taking into account the UAV's autonomies capacity. Two types of methods to solve this problem: *approximate methods* and *exact methods*. The exact methods implicitly consult all the possible solutions, which generates significant computation time. Therefore, they risk exponentially increasing when the size of the problem increases. On the other hand, approximate methods accept a margin of no optimality (approximate solution) with much less effort. Two approximate approaches are proposed in this work to solve this problem. Their development and details are presented in Secs. 3.3.1 and 3.3.2.

3.3.1. *POIs partition between UAVs and optimal path planning for each UAV*

To avoid collisions and redundancy, as well as to have a balanced effort between UAVs, we must ensure an efficient assignment of a subset of POIs for each UAV, while having satisfactory energetic optimality. We define a set of subgroups N_{uav} (according to the number of UAVs) which have $N_k|_{k=1,\dots,N_{\text{uav}}}$ POIs in one of each and $\sum_{k=1}^{N_{\text{uav}}} N_k = N$. In each subgroup, the N_k POIs have a minimum average distance between them, which will give compact subgroups around a focus (cluster). Thus, their geometric separation will help to avoid collisions. Such a situation is the most suitable for exploiting the principle of the k-means algorithm. The latter is summarized in Fig. 6.

In the last step of this first approach, we seek to find the best sequence to visit all the $N_k|_{k=1,\dots,N_{\text{uav}}}$ POIs assigned to each UAV, while minimizing the Total Path Length (TPL), starting from an initial point and returning to the same point. We call $\mathcal{P}_k$ the path connecting all these points. The objective function to be minimize is given as follows:

$$\mathcal{P}_{k_{\min}} = \sum_{k=1}^{N_{\text{uav}}} \sum_{i=1}^{N_k} d(c_i, c_{i+1}) + d(c_{N_k}, c_1), \tag{10}$$

where $d(c_i, c_{i+1})$ represents the Euclidean distance between the points c_i and c_{i+1}.

If we want to connect 10 points only as an example, we will have 181,440 and 362,880 possible cases for symmetric and asymmetrical configurations. This optimization problem is assimilated as a TSP, where its resolution is ensured by adapting GAs. In GAs, each POI is represented as a gene on a chromosome. The arrangement of these genes on the chromosome represents the order of visiting our POIs, including the first and the last genes representing the

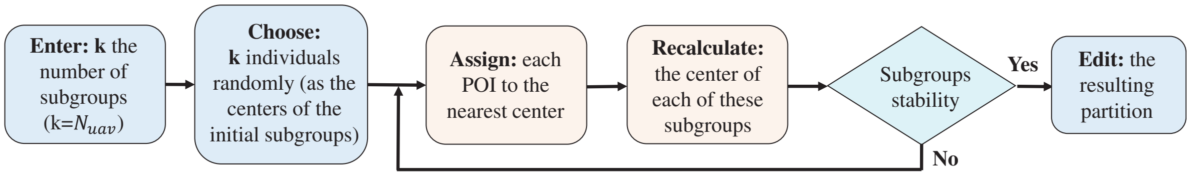

Fig. 6. POIs partition.

Algorithm 1. TSP-GAs

1: **Function**: **P=TSP GAs ( )**
2: **Initialization**: population size N_s, number of generations N_g, number of POIs N_k,
3: initial iterations $t = 1$, global min = Inf, initialize population Pop(t) with N_s chromosomes Pop$_i(t)$
4: **While** (not terminating condition) **do**
5: **for** $t \leftarrow 1$ to N_s **do**
6: $f_i \leftarrow f(\text{Pop}_i(t))$ % *f is the fitness function*
7: **for** $i \leftarrow 1$ to N_s **do**
8: NewPop$_i(t+1) \leftarrow$ rand choosePop$_i(t)$ from Pop$_i(t)$
9: CrossPop$(t+1) \leftarrow$ recombine(NewPop$(t+1)$) with P_c % *P_c is the crossover probability*
10: MutPop$(t+1) \leftarrow$ Mutate(CrossPop$(t+1)$) with P_m % *P_m is the mutation probability*
11: **Switch**
12: *Case 1* mutate by *flipping*
13: *Case 2* mutate by *swapping*
14: *Case 3* mutate by *sliding*
15: **Otherwise** *default*
16: Pop$(t+1) \leftarrow$ MutPop$(t+1)$
17: $t \leftarrow t+1$

starting point, where the UAVs turn back after finishing the mission. We developed this algorithm in Algorithm 1.

The algorithm considers N_s population of chromosomes (lines 2, 3). The fitness function is computed by the function $f(\text{Pop}_i(t))$, and it assigns a value f_i for each chromosome from the population (line 6). Then, new individuals are created by making certain genetic operations such as mutation and crossover to optimize n! possible permutations (lines 9, 10). Besides, swap operations (flip, slide and swap) in the mutation process are introduced (lines 1115). These operators accelerate the rearrangement of the POIs in the path, which quickly gives the best sequence of their visit, as well as they reduce the computation time and always give a solution even if the number of POIs is high. The algorithm updates the population with each iteration and it is executed for a terminating condition (line 4). It returns the cost of the best path, as well as the best order of the POIs.

3.3.2. *Path planning for all UAVs*

In this second approach, as in the first one, visiting the POIs resulting from the AOI decomposition by the UAVs is the primary objective for this step, while respecting the following rules:

- Taking measurements from all the POIs generated;
- The UAVs leave from the base station, visit one or more points and return to the same station;
- Each point is visited only by a single UAV and only once.

In this case, the problem is modeled as a VRP. Indeed, our POIs are considered as several customers who must be served by the UAVs from a single base station with known and equal requests. These requests represent an image of the time spent hovering to take the chemical substance concentration.

We consider a set $C_k = \{c_0, c_1, \ldots, c_i, \ldots, c_k, c_0\}$ as the $N_k|_{k=1\ldots N_{\text{uav}}}$ POIs assigned to the k^{th} UAV, with $c_0 = (x_0, y_0)$ represents the point of departure and arrival of all the UAVs, and straight lines connecting a POI to another are presented with a set of edges $E_k = (c_i, c_j) \mid c_i, c_j \in C_k, i \neq j$. Also, we associate for each followed path a graph $G_k = (C_k, E_k)$ containing C_k POIs and a set of E_k edges. The succession of visiting the POIs in each graph forms our desired path $\mathcal{P}_k$. Then, the symmetric Euclidean distance d_{ij} and $d_{ij} = d_{ji}, \forall i, j \in E$ is associated with each edge $(c_i, c_j) \in E$ as weight or cost. We specify the following data:

(a) Each POI from the set $C/\{c_0\}$ has an identical request $q_i = 1$ for the measurement time, and the load allocated for each UAV is $Q_k = \sum_{i=1}^{N_k} q_i$;
(b) The UAVs are identical with a limited capacity Q_{t_k} and $Q_{t_k} \leq Q_{t_{\max}}$ such as

$$\sum_{i \in C/\{c_0\}} q_i \leq Q_{t_{\max}} \times k. \tag{11}$$

We use also a decision variable x_e for each edge $(c_i, c_j) \in E$ and $x_e \in \{0, 1, 2\}$. Number "0" indicates that the edge is not visited by any UAV. Number "1" means that an UAV takes this edge once, and only the edges connecting only one POI which can have the value "2".

In the set of POIs $\xi \subseteq \mathcal{C}$, note $\delta(\xi)$ the set of edges $e \subseteq E$ that have one end, and $\delta(c_i)$ for a single node $i \subseteq \mathcal{C}$ rather than a set of nodes $\delta\{c_i\}$. Indeed, the mathematical model is

June 7, 2022 12:06:25pm WSPC/284-US 2250017 ISSN: 2301-3850 2nd Reading

formulated as follows:

$$\mathcal{F} = \min\left((1-\beta)[\alpha D_{\text{tot}} + (1-\alpha)\max(D_k)] + \beta\left[\text{mean}\left(\max\left(\frac{Q_{t_k}}{Q_{t_{\max}}} - 1, 0\right)\right)\right]\right). \tag{12}$$

For example

$$D_{\text{tot}} = \sum_{j=1}^{k} \sum_{i=1}^{N_k \in \mathbb{N}} x_e d_{ij}, \tag{13}$$

$$D_k = \sum_{l=1}^{N_k \in \mathbb{N}} x_e d_{ij}, \tag{14}$$

and

$$\sum_{e \in \delta(c_i)} x_e = 2, \quad \forall i \in \mathcal{C}/\{c_0\}, \tag{15}$$

$$\sum_{e \in \delta(c_0)} x_e = 2k, \tag{16}$$

$$\sum_{e \in \xi} x_e \leq |\xi| - 1, \quad \forall \xi \in E/\{c_0\}, \tag{17}$$

$$x_e \in \{0, 1\}, \quad \forall e \notin \delta(c_0), \tag{18}$$

$$x_e \in \{0, 1, 2\}, \quad \forall e \in \delta(c_0). \tag{19}$$

The objective function proposed is illustrated in Eq. (12). This cost function aims to minimize the UAV individual traveled distance D_k (Eq. (14)) and the total distance of the mission D_{tot} (Eq. (13)) on the one hand, and balanced sharing efforts between UAVs on the other hand. These factors to be optimized are balanced with weighting coefficients α and β.

Equation (15) explains how many times can we connect a POI with edges, and Eq. (16) models the UAV's turn back to the base station. Equation (17) prevents the closed paths without passing through the base station, while Eq. (18) means that all edges connecting a POI to another have taken one at maximum, the edges connecting a POI to the base station can take zero, one, or two times in the case of a back and forth for a single POI (Eq. (19)).

This system modeling our coverage mission is solved by establishing an efficient heuristic method called SA algorithm. Indeed, this last examines the neighboring solutions and preserves the best (intensification), and accepts more or less degraded solutions with a given probability for neighborhood solutions (diversification). Aside from leaving local minima, this allows us to explore a larger space of solutions. Such a concept is inspired from a physical principle in metallurgy, in which the process of cooling a metal is approached to have a more solid state of the placement of atoms [38]. We show the development of this technique in Algorithm 2.

Algorithm 2. TSP-GAs

1: **Function**: **R**=**SA** ( )
2: **Initialization**: $\mathcal{P} \leftarrow \mathcal{P}_0$, $T \leftarrow T_0$ % $\mathcal{P}_0$, T_0 *Initial solution (path) and Initial temperature respectively*
3: Temperature Damping Rate ($\mu = 0.98$), Define the stopping condition (ε),
4: Define a thermal equilibrium condition (or MaxIt)
5: **While** $t > \varepsilon$
6: **for** $it \leftarrow 1$ to MaxIt **do**
7: Extract randomly a Neighbor solution $\mathcal{P}^*$
8: using operator-based structure (**Swap**, **Reversion**, **Insertion**)
9: **If** $\mathcal{P}^*$ is better than $\mathcal{P}$ **then**
10: $\mathcal{P} \leftarrow \mathcal{P}^*$
11: **Else**
12: $\Delta f \leftarrow f(\mathcal{P}^*) - f(\mathcal{P})$
13: $\mathcal{P} \leftarrow \mathcal{P}^*$ with probability $Exp(-\Delta f/T)$
14: **End If**
15: **End for**
16: **Feasibility test** of the solution % *"Eq. (11)"*
17: $T \leftarrow T \times \mu$
18: **End while**
19: **Output**: *best path* $\mathcal{P}$, *Feasibility*

After choosing the initial conditions and specifying an initial solution respecting the mission constraints (lines 2–4), by small keys, we make local modifications to the order of our POIs in the path $\mathcal{P}$. At each iteration, we seek to decrease a dummy variable (temperature) to minimize the TPL (energy). The idea consists of keeping the new best neighboring solution, and accepting a less good solution with a probability. This probability is inversely proportional to this degradation, and proportional to the current temperature (lines 9–14). The probability decreases with the temperature lessening the more we advance in time. In this way, the algorithm readjusts the paths between them to have the best configuration, while escaping from the local minima and converges -if required- towards the total minimum.

The neighborhood exploration operators that change the order of visiting the POIs are ***Swap***, ***Reversion*** and ***Insertion***. These operators accelerate the convergence of the algorithm and/or minimize the computation time. We show the operations of these operators in Fig. 7.

This method adopted has excellent performance given the wide research space examined, its reduced computation time and very acceptable solution quality compared to the problem complexity.

3.4. *Gas distribution map*

Estimating gas dispersion from collected data in well-defined locations entails deriving a rule that simulates the

June 7, 2022 12:06:27pm WSPC/284-US 2250017 ISSN: 2301-3850 2nd Reading

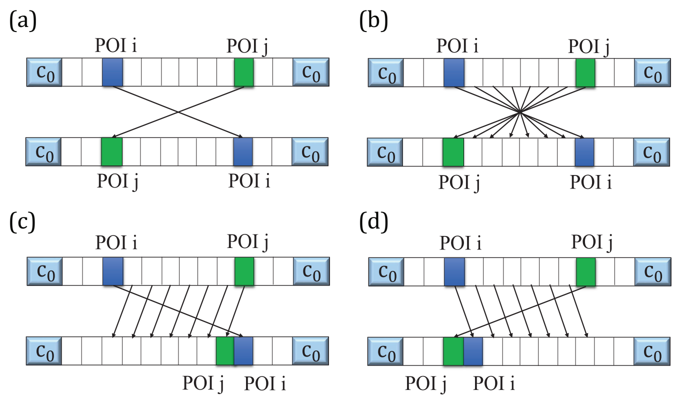

Fig. 7. *Swap*, *Reversion* and *Insertion* operators for SA: (a) Swap operation. (b) Reversion operation. (c) Insertion operator ($i < j$). (d) Insertion operator ($i > j$).

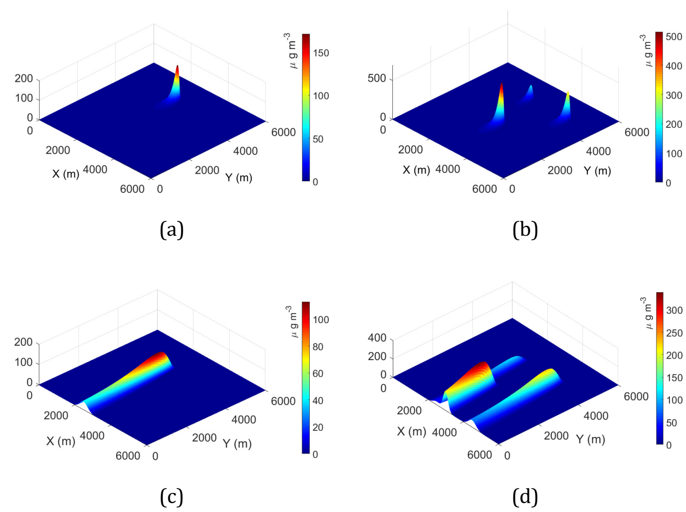

Fig. 8. Gas plume model (mean concentration): (a) and (b) One and three sources, respectively, in "A–B" stability class. (c) and (d) One and three sources, respectively, in "E–F" stability class.

studied phenomenon, and drawing conclusions about the evaluated sites (Sec. 2.1.). Indeed, when the locations of the POIs do not have a uniform or a regular grid, the procedure is called ***scattered data interpolation***.

We are based in this work on a method called ***Triangulation-based cubic interpolation*** [39]. This method uses a Delaunay triangulation [40] for our POIs, and a cubic spline fitted within each edge of the triangle. What gives a surface of $\mathcal{C}^2$ continuity class suited to the possible operations to identify the most likely source location. The objective of using such a method is to evaluate the helpfulness of the POIs distribution technique and the used coverage path planning approaches to rebuild the GDM, while without knowing the model and the type of the sources.

In Sec. 4, we will test the effectiveness of the proposed approaches, evaluating the influence of each parameter of the algorithms presented above, and we will discuss a variety of simulation results.

4. The Parameter Setting

We present in this section four simulation stages, reproducing the four stages of the methodology followed in Sec. 3, which allows us to visualize and facilitate the analysis of the proposed approaches. We present the sequence and data simulation in the following paragraphs.

The first stage of the simulation is the installation of a 2D workspace, in which we define our AOI. Indeed, this AOI has a polygon shape, situated on a square space of [6–6] Km of dimensions. In this region, we simulate one and three gas sources under different atmospheric conditions ("A–B" and "E–F" stability classes). In both cases, the wind speed is constant at 5 m/s from the direction of "0", $h = 50$ m. While $Q = 10$ g/s for the single source and $Q_1 = 10$ g/s, $Q_2 = 20$ g/s, and $Q_3 = 30$ g/s for the three sources, respectively. Figure 8 shows the simulated gas sources under the two atmospheric stability conditions.

In fact, while the wind speed and the emission rate are constant, this engenders a dispersion of the gas -time invariant- in an envelope of conical shape. This envelope extends more as we move farther away from the source. At the same time, the gas concentration decreases. The more the atmospheric conditions are stable ("E–F"), the more the concentration goes further (Figs. 8(c) and 8(d)).

Simulating multiple sources is the duplication of the same model, with their concentrations superimposed in the interference regions. This area is larger when the sources are close enough to each other, which can generate more complicated situations.

In the second stage, the POIs generation is common for two CPP suggested approaches, where four scenarios were simulated:

- In the first scenario, we used a 300 m radius of a circular sensor footprint with a coverage rate of $C_r = 0.9$, yielding 100 POIs.
- In the second one, we used a circular sensor footprint of 250 m of radius, with a coverage rate of $C_r = 1$, which gives almost 150 POIs.
- In the third scenario, we used a circular sensor footprint of 200 m of radius, with a coverage rate of $C_r = 1.2$, which gives 200 POIs.
- In the fourth scenario, we used a circular sensor footprint of 240 m of radius, with a coverage rate of $C_r = 1.5$, which gives 250 POIs.

For reasons of clarity, we show in Figs. 9(a) and 9(b) this second step presenting the sensor footprint, with the

June 7, 2022 12:06:39pm WSPC/284-US 2250017 ISSN: 2301-3850 2nd Reading

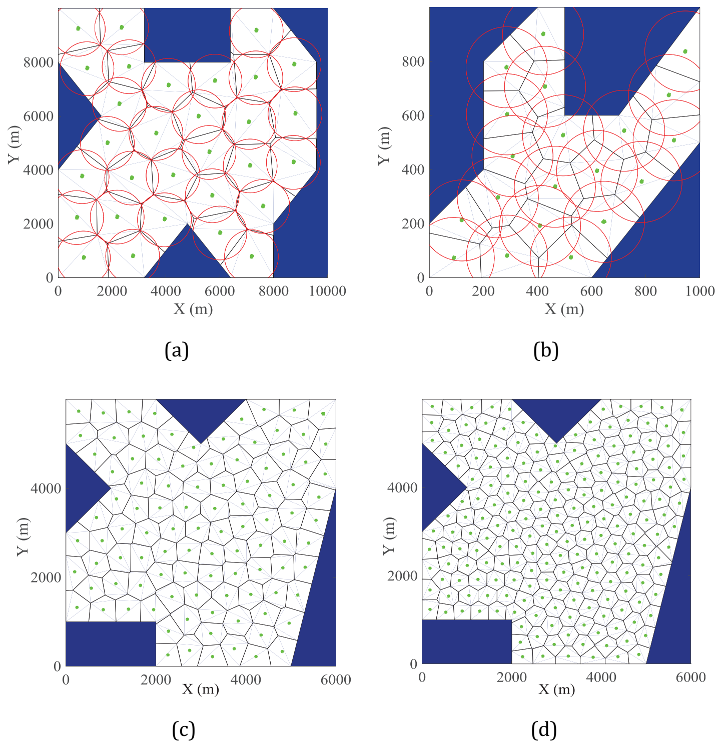

Fig. 9. POI's Generation and distribution: (a) 30 POIs and $R_{sf} = 1000$ m. (b) 20 POIs and $R_{sf} = 150$ m. (c) 100 POIs and $R_{sf} = 300$ m. (d) 200 POIs and $R_{sf} = 200$ m.

possibility of changing the size and the dimensions of the AOI. For the POI's deployment, we show only the first and the third scenarios in Figs. 9(c) and 9(d), respectively.

In the following stage, a homogeneous fleet (identical flight capacities) of different sizes is used to ensure the sample of the contaminant AOI, starting from the base station with coordinates $(x_0, y_0) = (2, 1)$ Km and returning to the same station.

In ***the first approach***, we assign the POIs to the UAVs after their grouping into isolated clusters, and subsequently calculate the optimal succession of their consultations.

For the first three scenarios (100 POIs, 150 POIs and 200 POIs), the POIs were inspected by three UAVs, then by five. In the last scenario, 250 POIs were inspected by five UAVs, then by eight. Figures 10–13 show the results of the first, second, third, and fourth *TSP-GAs* scenarios, respectively. Each one of them illustrates the POI's assignment, generated paths and the objective functions minimizing TPLs.

The number of generations N_g is adapted from one scenario to another. In fact, this choice is mostly influenced by the number of POIs assigned to each UAV, which decreases with the increase in the number of UAVs (for the same scenario) and increases from one scenario to another, due to the fact that we increase each time the total number of POIs. In this approach, the paths are planned in sequence (one by one), which requires fewer generations for each UAV. The total number of generations, however, is obtained by the multiplication of the above values by the number of UAVs.

Figure 14 shows the planned paths and cost function for the first and the second scenarios described above by applying ***the second approach*** (**VRP-SA**). Whereas Fig. 15 shows the planned paths and cost function for the third and the fourth scenarios. In this approach, the number of iterations is determined to ensure that the two techniques have the same algorithm complexity, allowing us to highlight comparison studies based on the same starting conditions.

In the last stage, the GDM is reconstructed (Sec. 3.4). At this stage, the map depends only on the number and the location of the POIs, and the values of the measures taken, where each measure is associated with a random error within the margin of $\pm 10\%$ of this measurement. Really, the results will be the same for both planning methods, the fact that we applied the same POI's generation technique. Finally, Figs. 16–19 show the GDM in the four scenarios (100 POIs, 150 POIs, 200 POIs and 250 POIs), respectively.

The simulation parameters in both approaches are illustrated in Table 1, whereas the total distances traveled and the number of POIs assigned for each UAV are

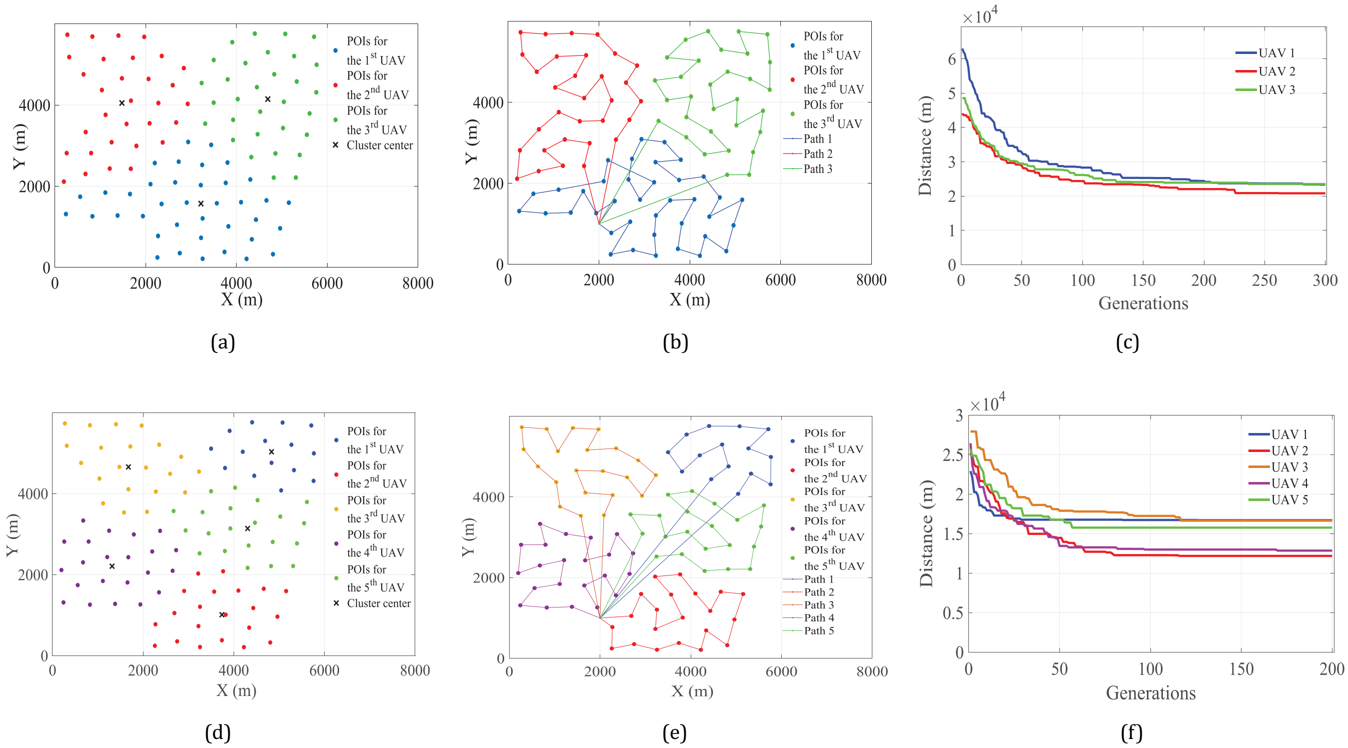

Fig. 10. CPP using *TSP-GAs* for 100 POIs (Scenario 1): (a), (d) POIs grouping in three and five clusters. (b), (e) Planned paths using three and five UAVs. (c), (f) TPLs according to generation (three and five UAVs, respectively).

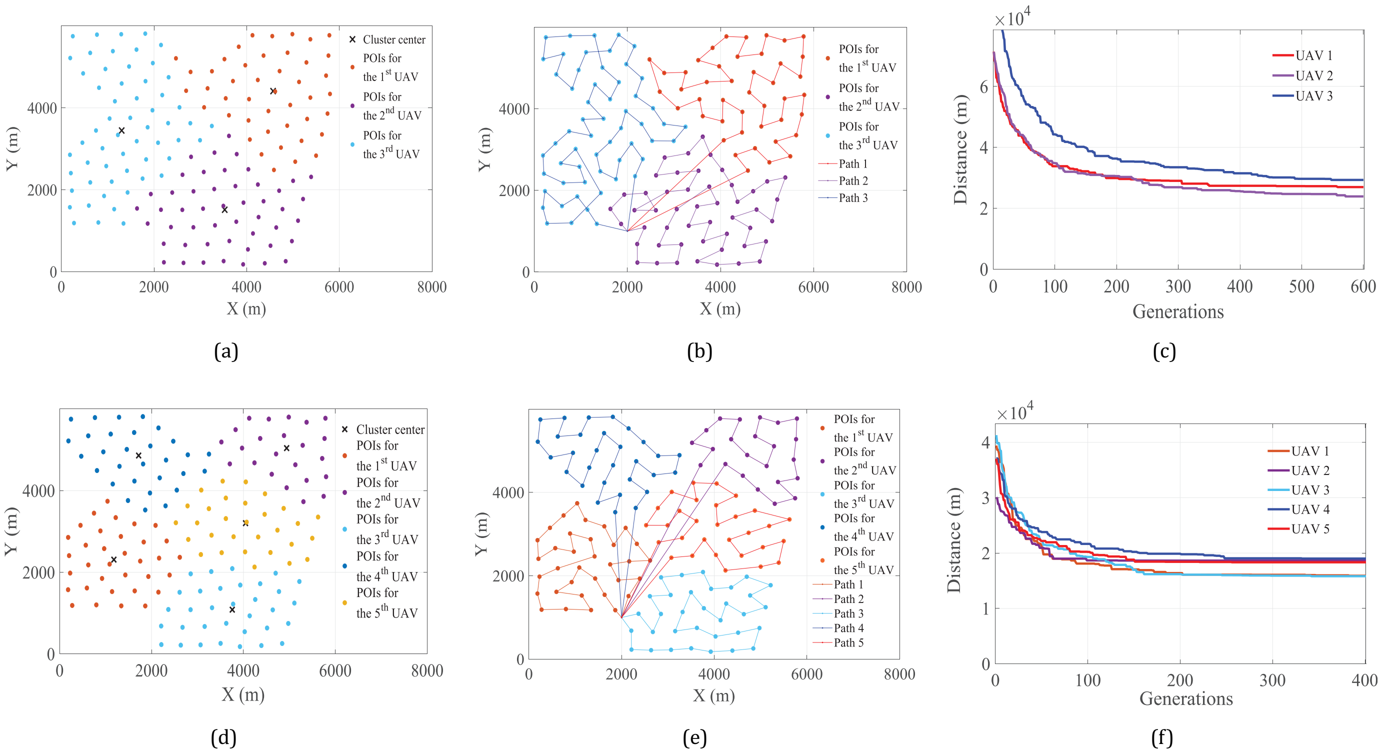

Fig. 11. CPP using *TSP-GAs* for 150 POIs (Scenario 2): (a), (d) POIs grouping in three and five clusters. (b), (e) Planned paths using three and five UAVs. (c), (f) TPLs according to generation (three and five UAVs, respectively).

June 7, 2022 12:07:29pm WSPC/284-US 2250017 ISSN: 2301-3850 2nd Reading

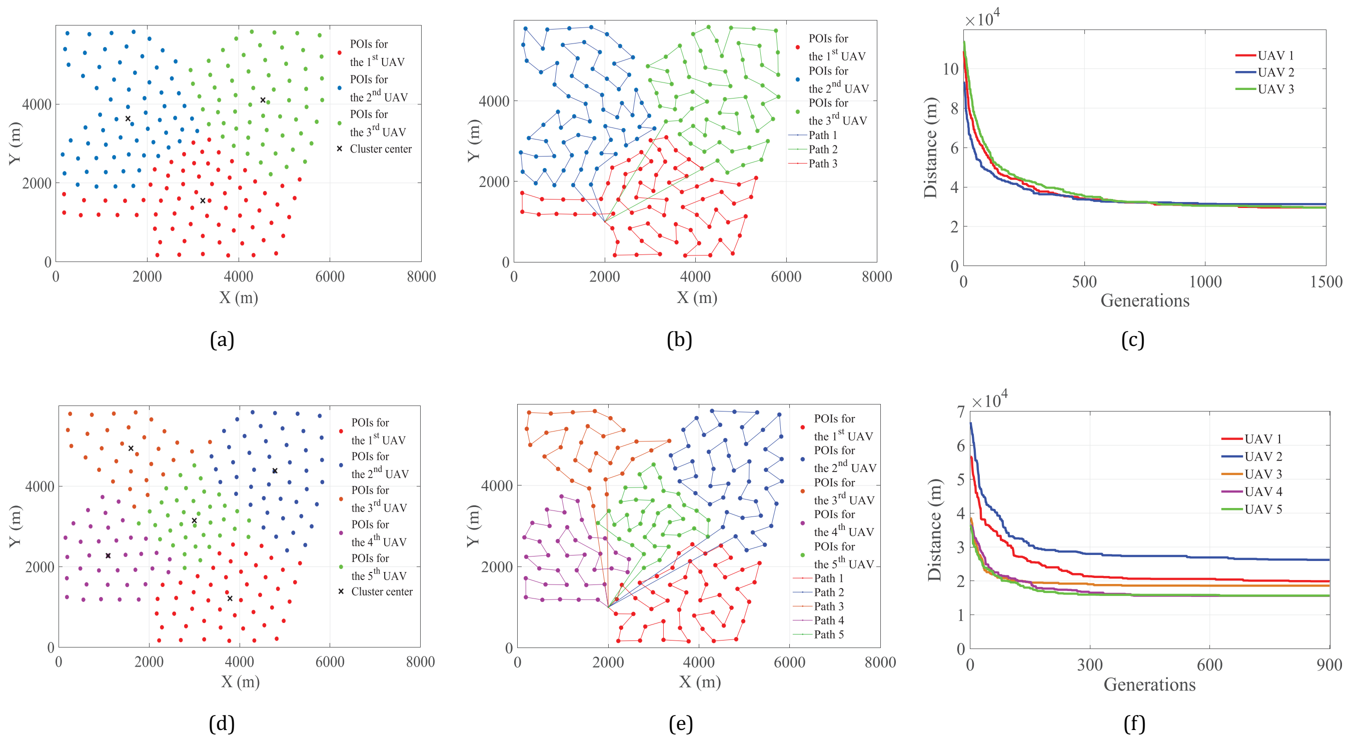

Fig. 12. CPP using *TSP-GAs* for 200 POIs (Scenario 3): (a), (d) POIs grouping in three and five clusters. (b), (e) Planned paths using three and five UAVs. (c), (f) TPLs according to generation (three and five UAVs, respectively).

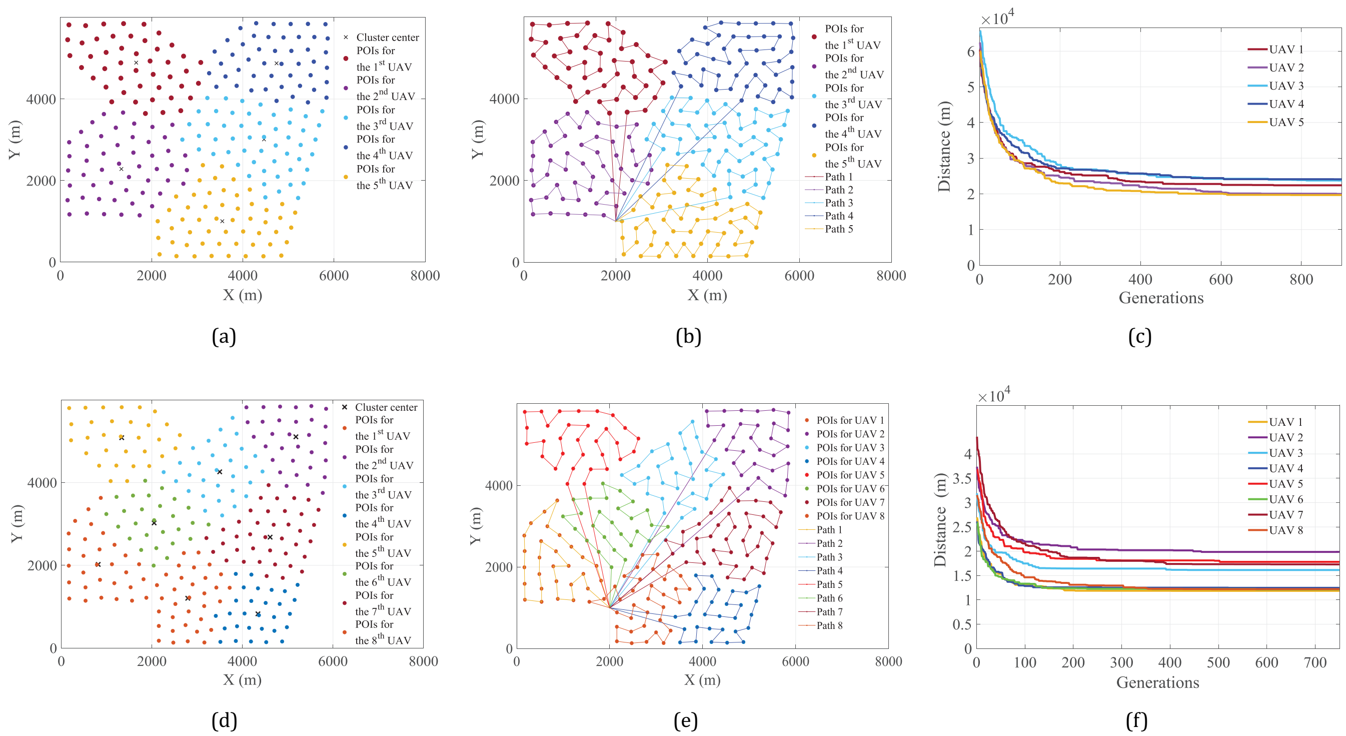

Fig. 13. CPP using *TSP-GAs* for 250 POIs (Scenario 4): (a), (d) POIs grouping in five and eight clusters. (b), (e) Planned paths using five and eight UAVs. (c), (f) TPLs according to generation (five and eight UAVs, respectively).

June 7, 2022 12:07:58pm WSPC/284-US 2250017 ISSN: 2301-3850 2nd Reading

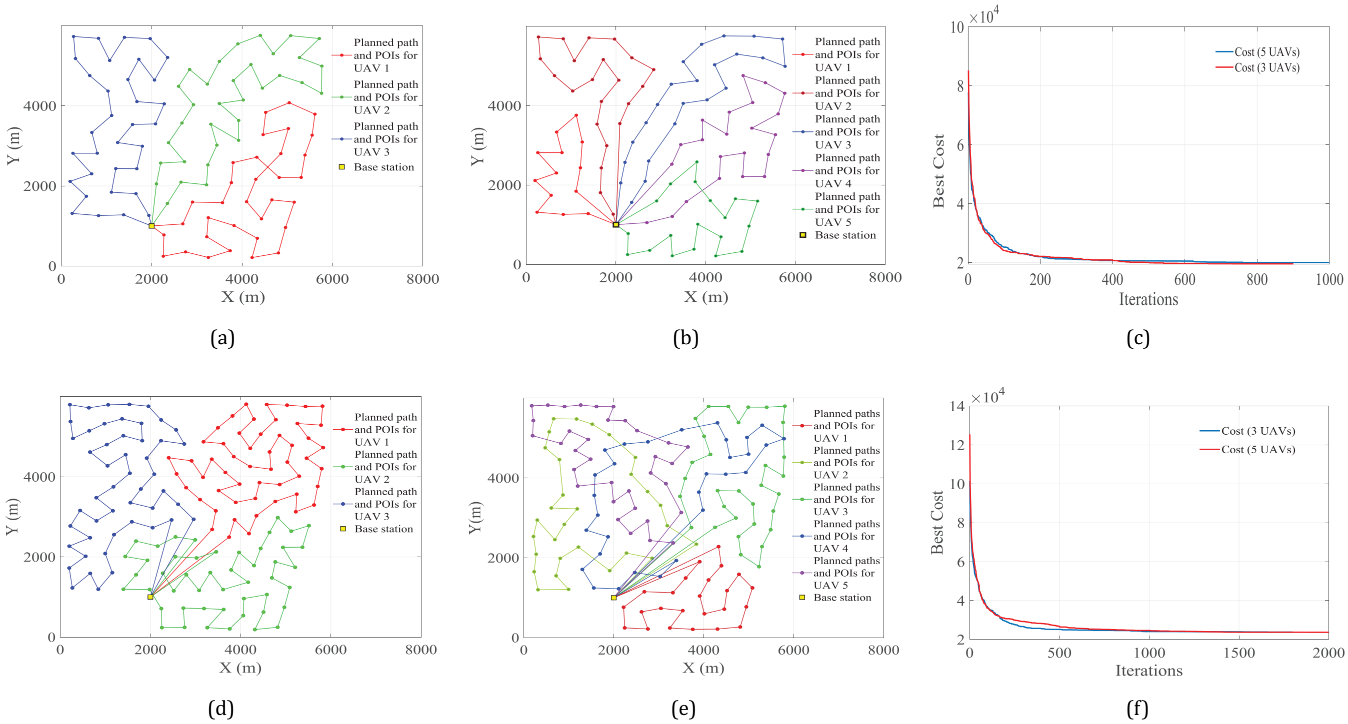

Fig. 14. CPP using *VRP-SA*: (a), (b) Planned paths using three and five UAVs, respectively (Scenario 1). (c) Cost function according to iterations (Scenario 1). (d), (e) Planned paths using three and five UAVs, respectively (Scenario 2). (f) Cost function according to iterations (Scenario 2).

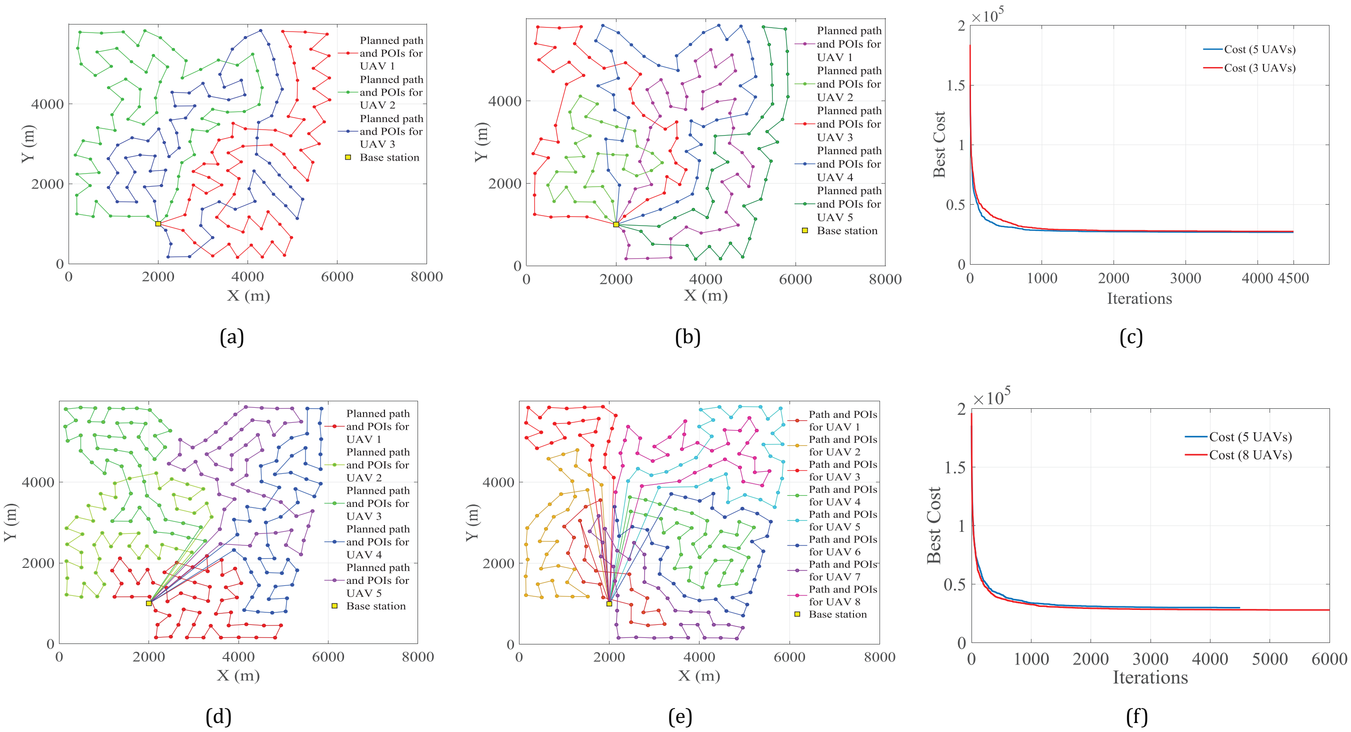

Fig. 15. CPP using *VRP-SA*: (a), (b) Planned paths using three and five UAVs, respectively (Scenario 3). (c) Cost function according to iterations (Scenario 3). (d), (e) Planned paths using five and eight UAVs, respectively (Scenario 4). (f) Cost function according to iterations (Scenario 4).

June 7, 2022 12:08:25pm WSPC/284-US 2250017 ISSN: 2301-3850 2nd Reading

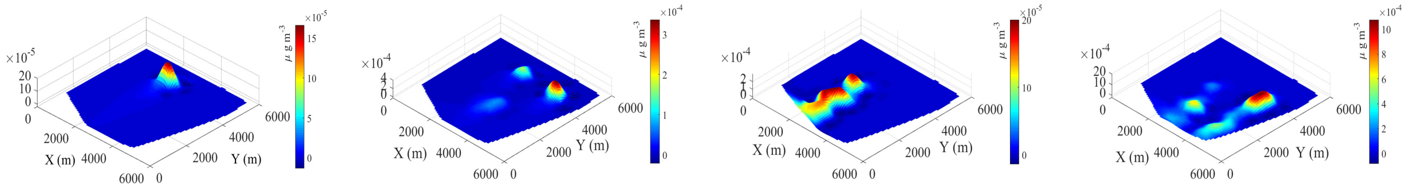

(a) (b) (c) (d)

Fig. 16. Gas distribution map basing on triangulation-based cubic interpolation (Scenario 1 (100 POIs)): (a), (b) One and three sources in "A–B" stability class, respectively. (c), (d) One and three sources in "E–F" stability class, respectively.

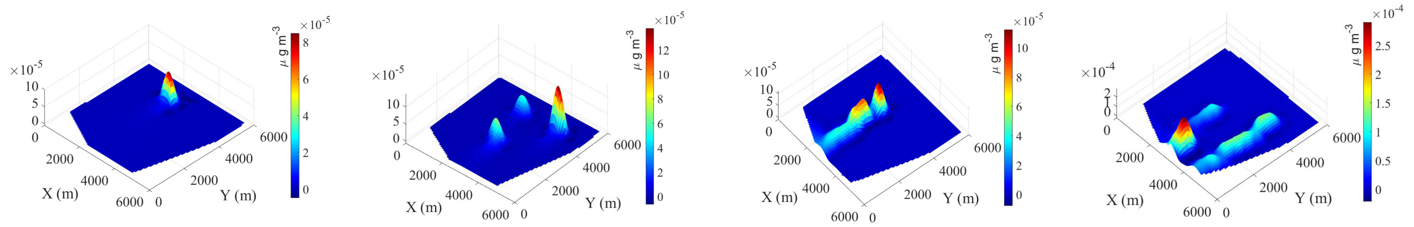

(a) (b) (c) (d)

Fig. 17. Gas distribution map basing on triangulation-based cubic interpolation (Scenario 2 (150 POIs)): (a), (b) One and three sources in "A–B" stability class, respectively. (c), (d) One and three sources in "E–F" stability class, respectively.

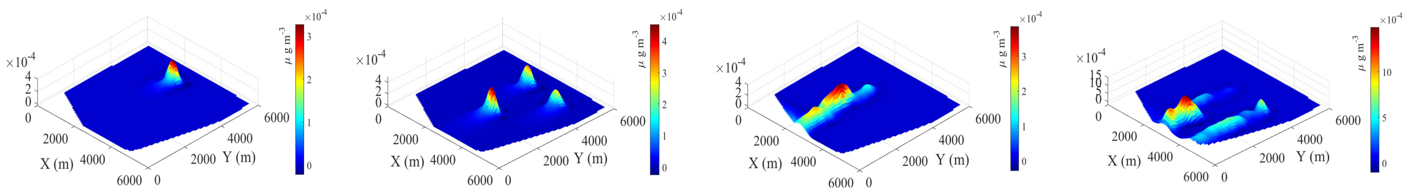

(a) (b) (c) (d)

Fig. 18. Gas distribution map basing on triangulation-based cubic interpolation (Scenario 3 (200 POIs)): (a), (b) One and three sources in "A–B" stability class, respectively. (c), (d) One and three sources in "E–F" stability class, respectively.

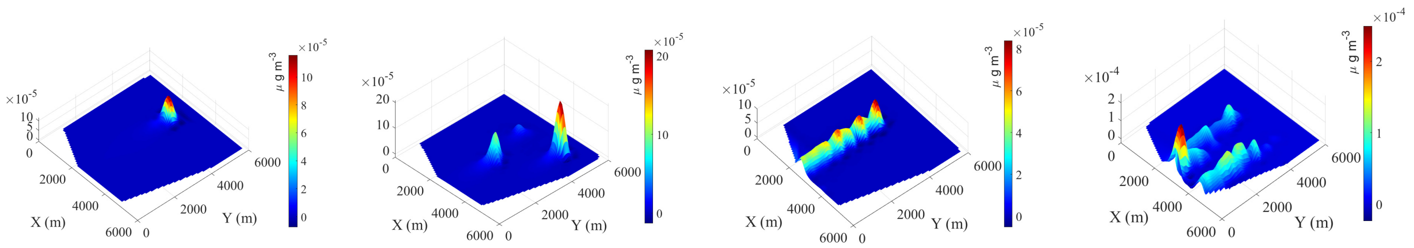

(a) (b) (c) (d)

Fig. 19. Gas distribution map basing on triangulation-based cubic interpolation (Scenario 4 (250 POIs)): (a), (b) One and three sources in "A–B" stability class, respectively. (c), (d) One and three sources in "E–F" stability class, respectively.

Table 1. Simulation parameters of the two approaches.

	POIs generation			TSP-GAs		VRP-SA $\mu = 0.98, \beta = \alpha = 0.5, T_0 = 100$	
	Number of POIs	Iterations	Number of UAVs	Population size N_s	Number of generations N_g	Iterations	UAVs capacities
Scenario 01 ($C_r = 0.9$)	100	50	03 05	80 80	300 200	900 1000	40 25
Scenario 02 ($C_r = 1$)	150	60	03 05	80 80	600 400	1800 2000	40 25
Scenario 03 ($C_r = 1.2$)	200	70	03 05	80 80	1500 900	4500 4500	70 45
Scenario 04 ($C_r = 1.5$)	250	80	05 08	80 80	900 750	4500 6000	70 40

Table 2. Traveled distances and the number of POIs assigned for each UAV in the first and the second scenarios.

Scenario	1st scenario (100 POIs)				2nd scenario (150 POIs)			
Number of UAVs	3 UAVs		5 UAVs		3 UAVs		5 UAVs	
Used approach	TSP-GAs	VRP-SA	TSP-GAs	VRP-SA	TSP-GAs	VRP-SA	TSP-GAs	VRP-SA
Distances (m)	23326 (38)	19470 (33)	16696 (15)	14948 (22)	26949 (44)	23845 (53)	15855 (34)	12388 (24)
and	20800 (31)	19845 (33)	12180 (21)	08883 (13)	23879 (49)	23672 (48)	18642 (23)	16493 (30)
	23505 (31)	19214 (34)	16637 (21)	11738 (19)	29294 (57)	23649 (49)	15682 (33)	15995 (32)
(Number of POIs)	—	—	12847 (22)	14934 (23)	—	—	18872 (30)	16607 (30)
	—	—	15755 (21)	14763 (23)	—	—	18039 (30)	16574 (34)
Total distances (m)	67631	58529	74115	65266	80122	71166	87090	78057

summarized in Table 2 for the first and second scenarios, and in Table 3 for the third and fourth scenarios.

5. Experiment Results and Discussion

The simulated environment is the place for planning paths to take samples. Indeed, the two proposed approaches use the same method to generate and locate our POIs. The latter requires more iterations as the number of POIs increases (depending on the desired coverage). Nevertheless, the POIs generated provide global and uniform coverage of the AOI, based on their optimal distribution along the surface of our AOI. In addition, the chosen size of the sensor footprint R_{sf} (also the coverage rate C_r) has a direct contribution to the number of POIs and the coverage resolution, as well as the reconstituted GDM.

The first method (TSP-GAs) shows good optimization performance, in a particularly homogeneous distribution of the POIs in each cluster, which has a beneficial effect on TPLs, as regards the choice of their number respecting the UAVs' flight capacities and the balanced division of the efforts between them (Tables 2 and 3), as well as this grouping at almost isolated paths each relative to the other, the good thing to avoid intersection points (collision avoidance for the same flight altitude).

In addition, the set of planned paths is optimized in terms of TPL (and/or energy consumed), feasible, and ensures the passage of all the POIs, hence the overall coverage of our AOI. Moreover, the free choice of the sensor footprint size, coverage rate, and the number of UAVs offers the possibility to apply this approach to various scenarios.

The use of GAs for the optimization in the first modeling gives a considerable effect on the solution optimality, as well as the acceleration of its convergence, considering the

Table 3. Traveled distances and the number of POIs assigned for each UAV in the third and the fourth scenarios.

Scenario	3rd scenario (200 POIs)				4th scenario (250 POIs)			
Number of UAVs	3 UAVs		5 UAVs		5 UAVs		8 UAVs	
Used approach	TSP-GAs	VRP-SA	TSP-GAs	VRP-SA	TSP-GAs	VRP-SA	TSP-GAs	VRP-SA
Distances (m)	29640 (67)	27566 (65)	19907 (48)	18971 (46)	22265 (46)	19153 (52)	11860 (28)	10521 (21)
and	29562 (71)	27396 (67)	15684 (37)	13318 (33)	19468 (51)	17937 (45)	19857 (31)	13671 (34)
(Number of POIs)	31331 (62)	27408 (68)	26215 (47)	18012 (40)	23222 (53)	19120 (51)	16138 (30)	10176 (26)
	—	—	18605 (31)	18663 (42)	23959 (47)	19533 (50)	12479 (29)	13997 (36)
	—	—	15634 (37)	19008 (39)	19226 (53)	19251 (52)	17816 (31)	13865 (33)
	—	—	—	—	—	—	12142 (27)	12769 (32)
	—	—	—	—	—	—	17295 (39)	13743 (34)
	—	—	—	—	—	—	12210 (35)	13633 (34)
Total distances (m)	90533	82370	96045	87972	108140	94994	119797	102375

initial size of the problem ($N_k!$, where N_k is the number of POIs in the cluster k).

The simulation results from the second approach (VRP-SA) show satisfactory planned paths. This is due to the objective function adopted, which has a positive effect on the balanced division of loads between UAVs. This is reflected in the number of POIs assigned to each UAV, and is returned also on the traveled distances almost equal (Tables 2 and 3). Increasing the number of iterations has a positive effect on the solution quality. On the other hand, this last is directly proportional to the size of the input vector (number of POIs and the number of UAVs). Although, this effect decreases with the exponential of the SA algorithm, i.e. exceeding a certain iteration number, the probability of having a better solution is greatly reduced. Lastly, a logic synthesis of how each drone's TPL can be reduced due to the fleet size increasing.

The initial parameters T_0, μ and ε must be properly established. It is necessary to ensure a slow decrease in the temperature in order to have an acceptable solution before its annulation. Furthermore, using insertion operators allows for a faster solution.

The two planning methods are strongly linked to the number of POIs selected (according to the desired coverage and the used sensor footprint). The problem becomes more complicated the more we increase their number, and both approaches require more iterations and/or computation time. However, the sum of the traveled distances by all UAVs in all cases is lower in VRP-SA (Tables 2 and 3). This is mainly caused by the first and the last path edges in TSP-GAs, which are longer to go from the base station to the distant clusters. As in this approach, each cluster is optimized independently of the others, which limits the choice of crossing points, hence the creation of this difference in TPLs. Conversely, in VRP-SA, the problem is seen as a whole, and the paths are optimized together. However, this difference in the sum of TPLs decreases more as the number of POIs increases and/or the number of UAVs decreases. In other words, as the number of POIs increases in each cluster, the more efficient the TSP-GAs method becomes.

The reconstituted GDM depends essentially on the number of measurement points (POIs), which defines its resolution. This is clearly demonstrated in Figs. 18 and 19 (scenarios 3 and 4) compared to Figs. 16 and 17 (scenarios 1 and 2), for one or three sources in both stability classes ("A–B" and "E–F"), which reveals clearly the most likely location of these sources (in relation to the reference sources shown in Fig. 8), as well as a better estimation of the dispersed quantities. In fact, the overall coverage of the AOI is very interesting, especially with the highest possible resolution.

6. Conclusion

We have seen in this work an integration of a plume model with two path planning approaches using a fleet of UAVs. The mission objective is to ensure the global coverage of an AOI containing chemical sources, in order to take and collect measurements over the whole of this area, and to estimate later how the chemical substance is distributed over this area.

To achieve this goal, we selected the outline of the region to be studied, and we simulated the gas sources using a gas plume model. The first step consists of generating and adequately distributing a set of POIs. Then, we plan optimized paths that ensure the passage of all these POIs by calculating the best sequence of their visits. In this step, two methods have been proposed. The first distributes the efforts between UAVs by assigning a subset of POIs to each one, where each subset is the result of grouping the POIs into clusters. Then, an optimal succession of visiting the POIs of each cluster separately is addressed, modeling the problem as a TSP, and solving it by GAs. The second planning approach models the problem as a VRP and solves it by taking advantage of the SA algorithm.

In both methods, the major advantages obtained from simulation tests consist in the selected number of POIs, which is derived from the used sensor footprint and the coverage rate. Furthermore, the choice of the shape and dimensions of the AOI, as well as the number of UAVs, provides greater flexibility. The use of GAs and SA algorithms and insertion operators gives optimization in TPLs and computation time. As a result, the POIs clustering and the chosen objective function for the SA algorithm provide a balanced sharing effort between UAVs, while respecting their flight capacities. In fact, these generic approaches can be exploited for many types of applications and a large number of scenarios, such as coverage for Unmanned Ground Vehicles (UGVs) and Underwater Vehicles (UVs). In terms of TPLs for UAVs, we can conclude that the second approach is more effective.

The last stage of our solution includes GDM reconstruction. Indeed, the triangulation-based cubic interpolation method is used. The selected method is suitable for further processing in order to locate the most promising positions of the gas sources, and possibly the delineation of the dispersion contour and predict its directions of propagation.

In future works, we will focus on guided planning for GSL while giving the same user information from the GDM. Then, we will go to the 3D generalization before their validation in real flight tests.

References

[1] B. P. Banerjee, S. Raval and P. J. Cullen, UAV-hyperspectral imaging of spectrally complex environments, *Int. J. Rem. Sens.* **41** (2020) 4136–4159.

[2] J. Su, M. Coombes, C. Liu, Y. Zhu, X. Song, S. Fang, L. Guo and W.-H. Chen, Machine learning-based crop drought mapping system by UAV remote sensing RGB imagery, *Unmanned Syst.* **08** (2020) 71–83.

[3] I. Maza and A. Ollero, Multiple UAV cooperative searching operation using polygon area decomposition and efficient coverage algorithms, *Distributed Autonomous Robotic Systems*, Vol. 6 (Springer, Japan, Tokyo, Tokyo, 2007), pp. 221–230.

[4] A. Barrientos, J. Colorado, J. D. Cerro, A. Martinez, C. Rossi, D. Sanz and J. Valente, Aerial remote sensing in agriculture: A practical approach to area coverage and path planning for fleets of mini aerial robots, *J. Field Robot.* **28**(5) (2011) 667–689.

[5] A. Mohiuddin, T. Tarek, Y. Zweiri and D. Gan, A survey of single and multi-UAV aerial manipulation, *Unmanned Syst.* **8**(2) (2020) 119–147.

[6] A. Sinha, A. Tsourdos and B. White, Multi UAV coordination for tracking the dispersion of a contaminant cloud in an urban region, *Euro. J. Control* **15** (2009) 441–448.

[7] M. Erdelj, E. Natalizio, K. R. Chowdhury and I. F. Akyildiz, Help from the Sky: Leveraging UAVs for disaster management, *IEEE Pervasive Comput.* **16** (2017) 24–32.

[8] P. Martin, J. Moore, J. Fardoulis, O. Payton and T. Scott, Radiological assessment on interest areas on the sellafield nuclear site via unmanned aerial vehicle, *Remote Sens.* **8** (2016) 913.

[9] P.-S. Murvay and I. Silea, A survey on gas leak detection and localization techniques, *J. Loss Prevent. Process Indust.* **25**(6) (2012) 966–973.

[10] T. F. Villa, F. Salimi, K. Morton, L. Morawska and F. Gonzalez, Development and validation of a UAV based system for air pollution measurements, *Sensors* **16**(12) (2016) 2202.

[11] J. Roldán, G. Joossen, D. Sanz, J. del Cerro and A. Barrientos, Mini-UAV-based sensory system for measuring environmental variables in greenhouses, *Sensors* **15** (2015) 3334–3350.

[12] J. Burgués, V. Hernández, A. J. Lilienthal and S. Marco, Smelling nano aerial vehicle for gas source localization and mapping, *Sensors* **19**(3) (2019) 478.

[13] G. Skorobogatov, C. Barrado and E. Salamí, Multiple UAV systems: A survey, *Unmanned Syst.* **08** (2020) 149–169.

[14] P. Neumann, S. Asadi, A. Lilienthal, M. Bartholmai and J. Schiller, Autonomous gas-sensitive microdrone: Wind vector estimation and gas distribution mapping, *IEEE Robot. Automat. Magaz.* **19** (2012) 50–61.

[15] A. J. Lilienthal, A. Loutfi and T. Duckett, Airborne chemical sensing with mobile robots, *Sensors* **6**(11) (2006) 1616–1678.

[16] G. Kowadlo and R. A. Russell, Robot odor localization: A taxonomy and survey, *Int. J. Robot. Res.* **27** (2008) 869–894.

[17] X.-X. Chen and J. Huang, Odor source localization algorithms on mobile robots: A review and future outlook, *Robot. Autonom. Syst.* **112** (2019) 123–136.

[18] T. Lochmatter, Bio-inspired and probabilistic algorithms for distributed odor source localization using mobile robots, Ph.D thesis, EPFL, Lausanne, Switzerland (2010).

[19] H. Ishida, K. Suetsugu, T. Nakamoto and T. Moriizumi, Study of autonomous mobile sensing system for localization of odor source using gas sensors and anemometric sensors, *Sensors Actuators A: Phys.* **45** (1994) 153–157.

[20] P. P. Neumann, V. Hernandez Bennetts, A. J. Lilienthal, M. Bartholmai and J. H. Schiller, Gas source localization with a micro-drone using bio-inspired and particle filter-based algorithms, *Adv. Robot.* **27** (2013) 725–738.

[21] H. Choset, Coverage for robotics: A survey of recent results, *Ann. Math. Artific. Intell.* **31** (2001) 113–126.

[22] J. Gibson, T. Schuler, L. McGuire, D. M. Lofaro and D. Sofge, Swarm and multi-agent time-based A* path planning for lighter-than-air systems, *Unmanned Syst.* **08** (2020) 253–260.

[23] E. Galceran and M. Carreras, A survey on coverage path planning for robotics, *Robot. Autonom. Syst.* **61** (2013) 1258–1276.

[24] M. Radmanesh, M. Kumar, P. H. Guentert and M. Sarim, Overview of path-planning and obstacle avoidance algorithms for UAVs: A comparative study, *Unmanned Syst.* **06** (2018) 95–118.

[25] T. Cabreira, L. Brisolara and P. R. FerreiraJr., Survey on coverage path planning with unmanned aerial vehicles, *Drones* **3** (2019) 4.

[26] M. D. Zollars, R. G. Cobb and D. J. Grymin, Optimal SUAS path planning in three-dimensional constrained environments, *Unmanned Syst.* **07** (2019) 105–118.

[27] H. Azpúrua, G. M. Freitas, D. G. Macharet and M. F. M. Campos, Multi-robot coverage path planning using hexagonal segmentation for geophysical surveys, *Robotica* **36** (2018) 1144–1166.

[28] F. Balampanis, I. Maza and A. Ollero, Coastal areas division and coverage with multiple UAVs for remote sensing, *Sensors* **17**(4) (2017) 808.

[29] G. Avellar, G. Pereira, L. Pimenta and P. Iscold, Multi-UAV routing for area coverage and remote sensing with minimum time, *Sensors* **15** (2015) 27783–27803.

[30] F. Causa, G. Fasano and M. Grassi, Multi-UAV path planning for autonomous missions in mixed GNSS coverage scenarios, *Sensors* **18** (2018) 4188.

[31] T. W. Horst, A surface depletion model for deposition from a Gaussian plume, *Atmospheric Environ.* **11** (1977) 41–46.

[32] J. C. Weil and R. P. Brower, An updated Gaussian Plume model for tall stacks, *J. Air Pollut. Contr. Assoc.* **34** (1984) 818–827.

[33] J. E. Sánchez-Sosa, J. Castillo-Mixcóatl, G. Beltrán-Pérez and S. Muñoz-Aguirre, An application of the Gaussian Plume model to localization of an indoor gas source with a mobile robot, *Sensors* **18**(12) (2018) 4375.

[34] P. Zannetti, Gaussian models, *Air Pollution Modeling* (Springer US, Boston, MA, 1990), pp. 141–183.

[35] D. B. Turner, *Workbook of Atmospheric Dispersion Estimates: An Introduction to Dispersion Modeling*, 2nd edn. (CRC Press, London, 2020).

[36] G. A. Briggs, Diffusion estimation for small emissions, *Atmospheric Turbulence and Diffusion Laboratory* **965** (1973) 83–145.

[37] Q. Du, V. Faber and M. Gunzburger, Centroidal voronoi tessellations: Applications and algorithms, *SIAM Rev.* **41** (1999) 637–676.

[38] S. Kirkpatrick, C. D. Gelatt and M. P. Vecchi, Optimization by simulated annealing, *Science* **220**(4598) (1983) 671–680.

[39] D. Watson*Contouring: A Guide to the Analysis and Display of Spatial Data* (Pergamon Elsevier Science, Tarrytown, 1992).

[40] A. Okabe, Spatial tessellations, *International Encyclopedia of Geography* (American Cancer Society, 2017), pp. 1–11.

Abdelwahhab Bouras received his engineering and the master degree in Automation and Guidance Systems from high school Ali Chabati, Algiers, Algeria (in 2013 and 2016, respectively). Currently, he is Ph.D. student in the laboratory of Complex Systems Control and Simulation (CSCS) at the Ecole Militaire Polytechnique (EMP), Bordj El Bahri, Algiers, Algeria. His research interests are in the areas of robotics and unmanned aerial vehicles, with a focus on robust control, path planning, trajectory planning, heuristic algorithms.

Yasser Bouzid received his engineering degree from the Ecole Militaire Polytechnique (EMP), Bordj El Bahri, Algiers, Algeria (in 2013) and the Master of Science (MSc) from the University of Paris XI, France (in 2015). He received his Ph.D. degree in Automatic from Paris Saclay University in 2018. He is currently Assistant Professor at the EMP and a member in the laboratory of Complex Systems Control and Simulation (CSCS). His research interests include nonlinear control, fault-tolerant control, observation and estimation, path planning, heuristic algorithms, unmanned aerial vehicles, mobile robots, multi-agent systems, soft robotics.

Mohamed Guiatni received his bachelor of engineering and Master of Science (MSc) degrees both from the Ecole Militaire Polytechnique (EMP), Bordj El Bahri, Algiers, Algeria and the PhD degree from the University of Evry, France in 2009. He is currently the Head of the Complex Systems Control and Simulation (CSCS) laboratory and Full Professor at the EMP. His research interests include haptic devices design and control, mechatronics, rehabilitation robotics, interactive simulation for military and medical applications, UAV design and control.